Acta Crystallographica Section B
Structural Science
ISSN 0108-7681

Order, disorder and structural modulations in Bi–Fe–W–O–Br Sillén–Aurivillius intergrowths

David Ávila-Brande,[a,b]* Ángel R. Landa-Cánovas[c] and L. Carlos Otero-Díaz[a,d]

[a]Departamento Química Inorgánica, Fac. CC. Químicas, Universidad Complutense, E-28040, Madrid, Spain, [b]Institut für Festkörperforschung and Ernst-Ruska-Centrum für Mikroskopie und Specktroskopie mit Elektronen, Forschungszentrum Jülich, 52425 Jülich, Germany, [c]Instituto Ciencia de Materiales de Madrid, CSIC, E-28049, Madrid, Spain, and [d]Centro de Microscopía, Universidad Complutense, E-28040, Madrid, Spain

Correspondence e-mail: d.avila@fz-juelich.de

Received 22 January 2008
Accepted 23 June 2008

Transmission electron microscopy observations on a new complex oxybromide with nominal composition $Bi_4Fe_{1/3}W_{2/3}O_8Br$, heated at high temperature, reveal the transformation of its basic structure yielding two types of crystals. The first crystal type shows ordered and disordered extended defects leading to a new family of intergrowths between one Sillén block and n Aurivillius blocks and occasionally between one Aurivillius block and n Sillén blocks. The second type presents a compositionally modulated structure, determined by electron diffraction, with an average composition $Bi_4Fe_{1/2}W_{1/2}O_{8-\delta}Br$ and unit-cell parameters $a = (1/\gamma)\,3.8$, $b = 3.8$, $c = 14.5$ Å ($\gamma = 0.10$–0.15) in the superspace group $Immm[(1-\gamma)00]$ no. 71.1.

1. Introduction

Phases with a perovskite structure have been extensively studied due to their chemical and structural flexibility (Mitchell, 2002), yielding a wealth of information on their electronic and magnetic properties including ferroelectricity, superconductivity (Wu *et al.*, 1987) and colossal magnetoresistence (Ramírez, 1997). This extensive range of properties has been exploited by industry, for example in their application as memory devices, capacitors, *etc*.

Within this family, the synthesis and characterization of layered perovskites have attracted an enormous amount of interest after the discovery of the high-temperature superconducting properties of YBaCuO (Ourmazd *et al.*, 1987; Hyde *et al.*, 1987) and the colossal magnetoresistence in manganites. The Aurivillius phases belong to the layered perovskites stacked along the (001) plane of the perovskite substructure. In general, their chemical composition can be described as $[Bi_2A_{n-1}B_nO_{3n+3}]$ or, for an easier comparison with other layered phases, as $[Bi_2O_2][A_{n-1}B_nO_{3n+1}]$. The $[Bi_2O_2]^{2+}$ sheet presents a PbO-type structure, *i.e.* square pyramids with the O atoms in the basal square plane and the bismuths in the apex pointing above and below the layer, interleaved with perovskite blocks $[A_{n-1}B_nO_{3n+1}]$ where n denotes the thickness of the block in terms of $\{BO_6\}$ octahedra (Wells, 1975; Aurivillius, 1949).

Up to now, the most important physical property of these phases has been their ferroelectric behaviour with long spontaneous polarization (Scott, 1998) and high Curie temperatures (Scott, 1995). However, the intrinsic chemical flexibility of the basic perovskite structure of this system suggests that by inserting the appropriate transition metal in the perovskite layer, new phases with promising multiferroic properties can be obtained.

Similar layer structures have been found for a number of bismuth oxide compounds. The common structural element in

all these compounds is the square-planar (Bi_2O_2) layers between which halides or certain radical layers are inserted. The first of these compounds were synthesized and characterized by Sillén *et al.* (Wilson, 1947) and can be described as the stacking of (Bi_2O_2) layers and one, two or, rarely, three halide sheets: $[Bi_2O_2][X_m]$, m = 1, 2 or 3.

The Sillén phases have been shown to react with a number of the Aurivillius family members to form intergrowth compounds $[Bi_2O_2][A_{n-1}B_nO_{3n+1}][Bi_2O_2][X_m]$. The ideal space group of these intergrowths is $P4/mmm$, but they are usually distorted, showing lower symmetry. Aurivillius reported the synthesis of large numbers of compounds $[Bi_2O_2][A_{n-1}B_nO_{3n+1}][Bi_2O_2][X]$ with n = 1–4 (Aurivillius, 1984). Later on, Ackerman revised these compounds, refining the structure of the simplest members Bi_4NbO_8Cl and $PbBi_3WO_8Cl$ by X-ray single-crystal data (Ackerman, 1986). Recently, Kusainova *et al.* re-analysed the structure of Bi_4NbO_8Cl by neutron powder diffraction and studied its ferroelectric properties, yielding a T_c of 465 K (Kusainova *et al.*, 2001). The first observations on these kinds of materials at the atomic level were performed by Ávila-Brande *et al.* over the series of compounds $Bi_4M_xW_{1-x}O_{8-\delta}X$ (M: Ti^{4+}, Mn^{3+}, Cu^{2+}; X: Cl, Br; Ávila-Brande, 2006; Ávila-Brande *et al.*, 2005, 2006, 2007). For example, the structure of the compound $Bi_4Mn_{1/3}W_{2/3}O_8Cl$ was determined by a combination of selected area electron diffraction (SAED), microdiffraction and exit wave reconstruction (EWR), leading to a structural model which was refined using X-ray diffraction data (Ávila-Brande *et al.*, 2006). The combination of EWR and statistical parameter estimations has allowed us to refine the local structure with a precision in the picometre range (Bals *et al.*, 2006). In addition, we have reported the synthesis and structure determination of the first Sillén–BICUWOX intergrowth $Bi_4Cu_{1/3}W_{2/3}O_{8-\delta}Cl$, showing the local position of the oxygen vacancies on the phase image of the reconstructed wave (Ávila-Brande *et al.*, 2007).

Following the study of this kind of layered compounds, the aim of this work was the structural determination of a new Sillén–Aurivillius oxybromide $Bi_4Fe_{1/3}W_{2/3}O_8Br$ and its evolution when heated at moderately high temperatures (1473 K).

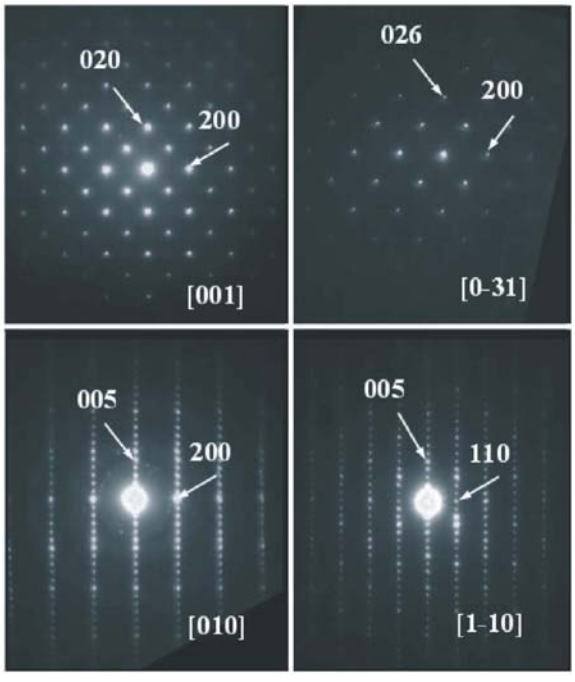

Figure 1
SAED patterns along the zone axes [001], [0$\bar{3}$1], [010] and [1$\bar{1}$0] for the $Bi_4Fe_{1/3}W_{2/3}O_8Br$ phase, indexed in orthorhombic symmetry.

2. Experimental details

A polycrystalline sample with nominal composition $Bi_4Fe_{1/3}W_{2/3}O_8Br$ was prepared by heating the stoichiometric amounts of the oxides Bi_2O_3 (99.99%), WO_3 (99.99%), Fe_2O_3 (99.99%) and BiOBr at 993 K for a week in an evacuated (P = 133.322 × 10^{-4} Pa) sealed silica tube. The sample was then cooled in 8 h to room temperature by switching off the furnace.

The synthesis of non-commercial BiOBr was carried out by dissolving Bi_2O_3 (99.99%) in HBr (47%) until saturation, with further hydrolysis with hot water (Brauer, 1963). The product was filtered, washed and finally dried at 473 K for 4 d. The single-phase nature of the BiOBr product was confirmed by X-ray powder diffraction.

A portion of the synthesized compound was then fired at 1473 K in a sealed platinum tube for 30 min. After this time the furnace was switched off.

Samples for transmission electron microscopy (TEM) were prepared by ultrasonic dispersion of the crystals in *n*-butanol. Drops of this dispersion were deposited on a holey carbon-coated copper grid. A JEOL 2000FX equipped with a LINK ISIS 300 analyser was used for XEDS (X-ray energy dispersive spectroscopy) analysis, microdiffraction and SAED. High-resolution electron microscopy (HREM) was performed using a JEOL 3000 F TEM. HREM image simulations were performed using *MacTempas* software (Kilaas, 1987).

X-ray powder diffraction patterns (XRPD) were recorded on a Siemens D-501 (Cu $K\alpha_1$ radiation, λ = 1.5406 Å) over the angular range 10–100°, with a step scan of 0.04°.

Magnetic susceptibility measurements were performed on polycrystalline samples between 2 and 300 K, using a Quantum Design SQUID MPMS-X.

3. Results

3.1. Microstructural study of $Bi_4Fe_{1/3}W_{2/3}O_8Br$

A nearly pure brown sample was obtained from the synthetic route described above. Bi_2WO_6 and $Bi_{24}O_{31}Br_{10}$ were detected as minor impurities by XRPD and TEM.

The SAED in Fig. 1 is consistent either with a primitive P tetragonal unit cell (a_o = b_o = 3.8 Å and c_o = 14.5 Å) or a pseudotetragonal one [$a \simeq b = (2a_o)^{1/2}$ = 5.4 Å and c = 14.5 Å] with C centring (hkl: $h + k = 2n + 1$). Due to the equivalence between a primitive or a C-centred unit cell [a P cell is equivalent to a C-centred $(2a_o)^{1/2}$, $(2b_o)^{1/2}$ unit cell] SAED

cannot distinguish between the two cases. However, using convergent-beam electron diffraction patterns (CBED) the point group of a space group can be determined by observing the ideal symmetry of CBED patterns. The zero-order Laue zone (ZOLZ) ideal symmetry for a tetragonal system along [001] is characterized by a fourfold axis. However, the CBED pattern taken along [001] (Fig. 2) shows a diffraction group $m1_R$ (Tanaka & Terauchi, 1985), characterized by one vertical mirror (m_v), a mirror plane (m_2) parallel to the plane of projection and a twofold rotation axis (2) also parallel to the plane of projection. This diffraction group $m1_R$ is in agreement with the orthorhombic space group *Cm2m* (standard group *Amm2* no. 38). Neither extra reflections nor streaking were found, indicating a well ordered layered structure. In this case, taking into account only the XRPD data, the parameters can be refined in a tetragonal unit cell [a = 3.874 (5), c = 14.554 (1) Å] in the space group *P4/mmm,* but the real symmetry determined by SAED and CBED indicates the orthorhombic one.

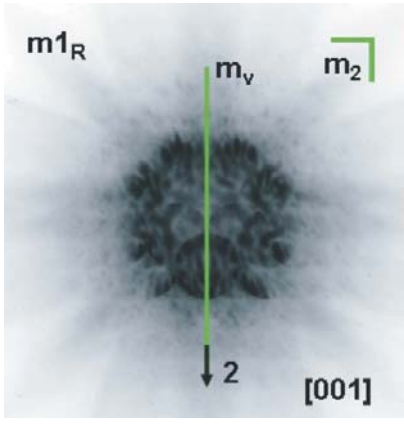

Figure 2
Bright field (BF) CBED pattern taken along the [001] zone axis showing $m1_R$ diffraction symmetry.

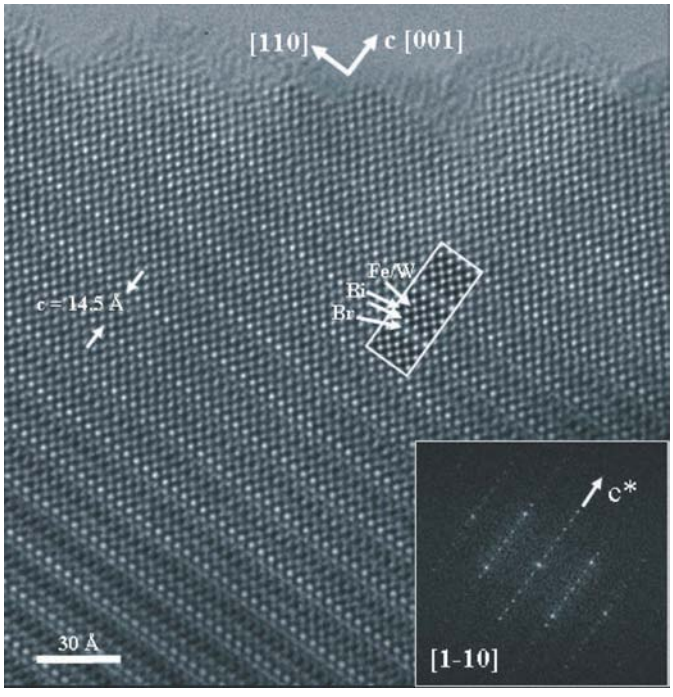

Figure 3
Experimental HREM of one crystal of the $Bi_4Fe_{1/3}W_{2/3}O_8Br$ phase along the [1$\bar{1}$0] zone axis. Note the good match between the experimental and the simulated image (boxed in white) calculated for a defocus of Δf = −200 Å and a thickness of t = 10 Å.

The unit-cell parameters determined after SAED were refined using X-ray powder diffraction data and Si (5 N) as an internal standard yielded the values a = 5.479 (2), b = 5.479 (7) and c = 14.554 (1) Å.

EDS (energy-dispersive spectroscopy) analyses performed on three points of each of 15 microcrystallites yielded an average composition of $Bi_{3.95\ (4)}Fe_{0.35\ (3)}W_{0.67\ (2)}Br_{1.02\ (2)}$, in good agreement with the nominal one.

In order to confirm the degree of ordering of this new phase, a HREM study was carried out. A structural image along the [1$\bar{1}$0] zone axis is displayed in Fig. 3, showing a regular stacking along c with 14.5 Å periodicity corresponding to c or the stacking axis. The simulated image, using the model from the isostructural compound $Bi_4Mn_{1/3}W_{2/3}O_8Cl$ (Ávila-Brande *et al.*, 2006) and calculated for a defocus value of Δf = −200 Å and a thickness of t = 10 Å, was found to be in good agreement with the experimental one and is inserted in the HREM image. Near to the Scherzer defocus, dark dots indicate the different ions; however, in this case, due to the stronger scattering factor of Br we cannot directly identify the halide layer as previously done with Cl (Ávila-Brande *et al.*, 2006) in $Bi_4Ti_{1/2}W_{1/2}O_8Cl$. Only after the image simulations were we able to identify the different atoms with the dots as marked in the image.

3.2. Magnetic measurements of $Bi_4Fe_{1/3}W_{2/3}O_8Br$

Fig. 4 shows the magnetic susceptibility variation with temperature, with the $1/\chi$ *versus* T curve shown as an inset.

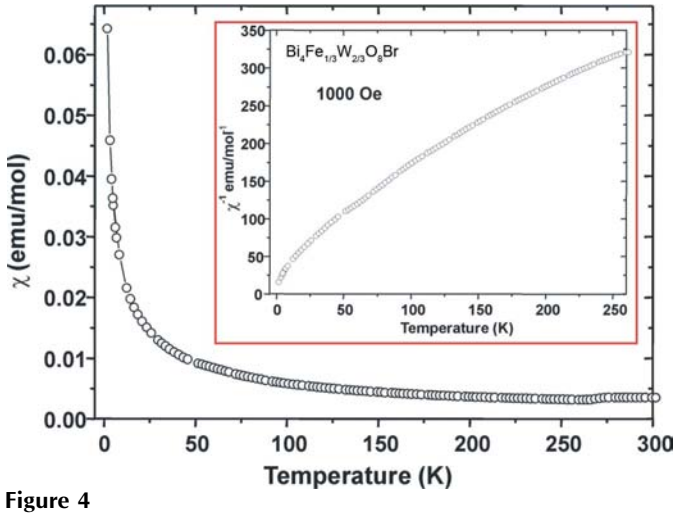

Figure 4
Plot of the magnetic susceptibility *versus* temperature. The inset shows the χ^{-1} curve for the sample.

Table 1
New family of oxyhalides determined from HRTEM observations.

n	Composition	c axis (Å)
1	$(Bi_2O_2Br)(Bi_2Fe_{1/3}W_{2/3}O_6)$	14.5
2	$(Bi_2O_2Br)(Bi_2Fe_{1/5}W_{4/5}O_6)_2$	45.5
3	$(Bi_2O_2Br)(Bi_2Fe_{1/7}W_{6/7}O_6)_3$	31.5
∞	Bi_2WO_6	16.4
n	$(Bi_2O_2Br)[Bi_2Fe_{1/(2n+1)}W_{2n/(2n+1)}O_6]_n$	–

This compound exhibits paramagnetic behaviour in the whole temperature range. It shows a slight curvature which approximately obeys the Curie–Weiss law between 160 and 280 K with μ_{eff} = 5.20 μ_B. The only cation with a magnetic moment in the compound $Bi_4Fe_{1/3}W_{2/3}O_8Br$ is Fe^{3+}; its theoretical moment corresponding to a high-spin configuration is 5.91 μ_B, whereas in low-spin configuration the effective value is 1.73 μ_B (Smart & Moore, 1992). The experimental moment corresponds to a high-spin Fe^{3+}; however, this value decreases when the temperature is lowered. This behaviour can be interpreted as a gradual transition from a high-spin to a low-spin configuration (Gütlich & Hauser, 1990).

3.3. Structural segregation of $Bi_4Fe_{1/3}W_{2/3}O_8Br$ at high temperature

Because of the presence of impurities in our powdered sample, we tried to grow single crystals by heating a small portion of the powder in a sealed platinum tube at 1473 K. The synthesized sample was multiphase with a large amount of disorder and, therefore, not suitable for X-ray powder diffraction refinements. Furthermore, the crystals obtained were too small for single-crystal measurements, but the electron microscopy observations have shown that, in spite of the majority of crystals belonging to the starting phase, some crystals exhibited extended defects and a new phase with modulated structure was also found.

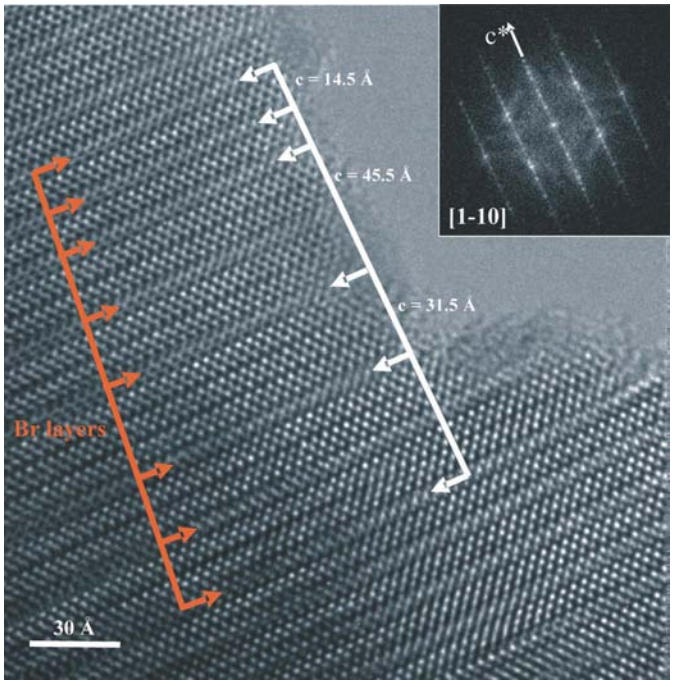

Figure 5
HRTEM image along [1$\bar{1}$0] of a crystal heated at 1473 K showing the members n = 1 ($c \simeq$ 14.5 Å), n = 2 ($c \simeq$ 45.5 Å) and n = 3 ($c \simeq$ 31.5 Å) of the family with the general composition $(Bi_2O_2Br)[Bi_2Fe_{1/(2n+1)}W_{2n/(2n+1)}O_6]_n$. The white arrows indicate the different unit cells observed in the crystal as disordered intergrowth, whereas the orange ones mark the bromine layers.

3.3.1. Disordered intergrowths. As described above, thermal treatment of the starting compound gives rise to two kinds of closely related phases. In this section we describe the electron microscopy observations made on several defective crystals. Fig. 5 shows a HRTEM image taken along the [1$\bar{1}$0] zone axis where extended defects are clearly observed. The power spectrum inserted in the upper part of this micrograph presents the same basic pattern found in $Bi_4Fe_{1/3}W_{2/3}O_8Br$, but the presence of streaking along the diffraction maxima rows parallel to c^* indicates disorder perpendicular to the stacking axis.

In the upper and lower parts of this image, we find periodicities of 14.5 Å between the brighter bromine layers, arrowed in orange in the left part of the image, corresponding to the c axis of the starting compound $Bi_4Fe_{1/3}W_{2/3}O_8Br$. In the middle part, we can also measure periodicities of 31.5 and 45.5 Å. The same situation was previously observed in the structural study of $Bi_4Cu_{1/3}W_{2/3}O_{8-\delta}Cl$ (Ávila-Brande *et al.*, 2007) and these extended defects were explained by the substitution of one halide layer for n $[Bi_2O_2][MO_{4-\delta}]$ blocks during the stacking process, giving rise to a new family of compounds described as the intergrowth between one $[Bi_2O_2Br]$ block and n $[Bi_2(W/Fe)O_6]$ slabs (see Table 1). These defects can be understood by the substitution of one bromine layer $[Br]^-$ by octahedral layers $[Fe/WO_4]^{3-}$, thus

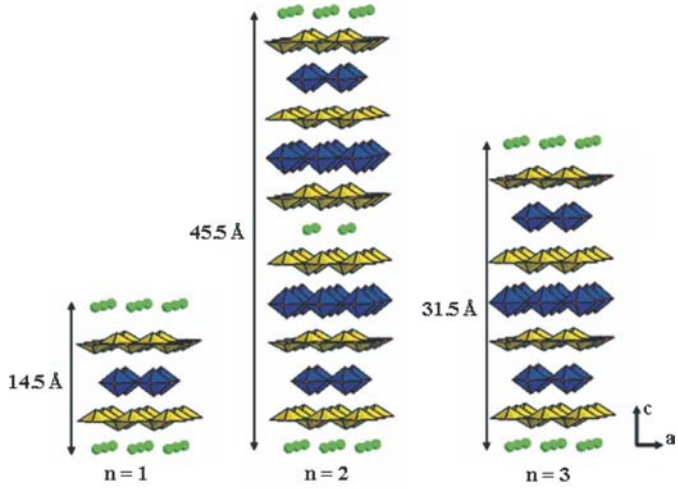

Figure 6
Ideal structural models for the phases $(Bi_2O_2Br)[Bi_2Fe_{1/(2n+1)}W_{2n/(2n+1)}O_6]_n$ with n = 1–3 identified by HRTEM. Green circles indicate Br^- anions, BiO_4 square pyramids are depicted in yellow and MO_6 octahedra in blue.

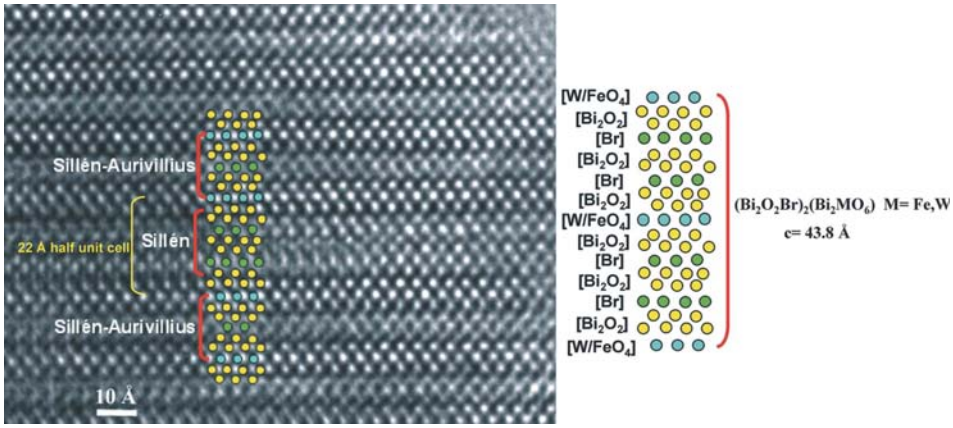

Figure 7
HRTEM image showing the intergrowth between two $[Bi_2O_2Br]$ slabs and one Aurivillius $[Bi_2(W/Fe)O_6]$. On the right an atomic model is included.

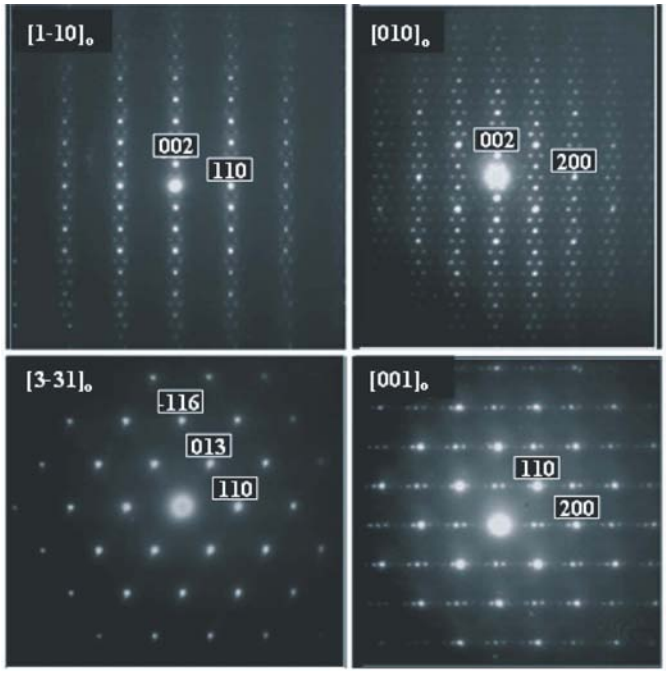

Figure 8
SAED patterns along the zone axes $[1\bar{1}0]_o$, $[010]_o$, $[3\bar{3}1]_o$ and $[001]_o$ of the modulated phase. The strong maxima of the patterns have been indexed in the base of an orthorhombic subcell denoted by the subscript o.

increasing the negative charge. To make an electroneutral compound the amount of Fe^{3+} should decrease in favour of W^{6+}, yielding the theoretical Fe:W ratio displayed in Table 1. We tried to measure the Fe:W ratio using a 10 nm electron probe, but the fast decomposition of these crystals when the probe was converged made measurement of realistic ratios impossible. However, the amount of Fe was always lower than in the $n = 1$ crystals.

The existence of the members $n = 1$–3 is clearly shown by the HRTEM image of Fig. 5 where we can see the disordered intergrowth of these three members. The ideal structural models for those phases are depicted in Fig. 6.

Since the combination described above is possible, the reverse kind of intergrowth is also possible, *i.e.* the intergrowth between n $[Bi_2O_2Br]$ Sillén slabs and one Aurivillius $[Bi_2(W/Fe)O_6]$ block yielding another new family $(Bi_2O_2Br)_n(Bi_2Fe_{2/3}W_{1/3}O_6)$. This situation seems less favourable due to the weaker bond between the halide and bismuth, with bond distances ranging from 3.26 to 3.41 Å (Ávila-Brande *et al.*, 2006), compared with the shorter distances between metal–apical oxygen–halide in the more stable Aurivillius block. However, we have also found one crystal where half the unit cell of the member $n = 2$ is inserted into the dominant phase (see Fig. 7).

3.3.2. New modulated structure related to $Bi_4Fe_{1/3}W_{2/3}O_8Br$. *Study of the reciprocal space*: The second type of crystals we found in the sample exhibit more complex electron diffraction patterns, as shown in Fig. 8. These patterns were recorded along $[1\bar{1}0]_o$, $[010]_o$, $[3\bar{3}1]_o$ and $[001]_o$, where the subscript o denotes the basic orthorhombic unit cell ($a \simeq b \simeq a_p \simeq 3.8$ and $c \simeq 14.5$ Å). It is obvious that, apart from the strong basic reflections, a large number of additional weak diffraction maxima, which are incommensurate with the basic lattice, are observed along the $[010]_o$, $[1\bar{1}0]_o$ and $[001]_o$ zone axes. Such diffraction patterns can be indexed in terms of a strong set of matrix reflections characteristic of the average basic lattice and a weaker set of satellite reflections by means of the reciprocal lattice vector $\mathbf{G} = h\mathbf{a}^* + k\mathbf{b}^* + l\mathbf{c}^* + m\mathbf{q}$ (de Wolff *et al.*, 1981; Withers, 1989), where m is an integer and $\mathbf{q}$ the primary modulation wavevector. The most intense or basic reflections correspond to an orthorhombic unit cell with the following lattice parameters $\mathbf{a} \simeq \mathbf{b} \simeq \mathbf{a}_p \simeq 3.8$ Å and $\mathbf{c} \simeq 14.5$ Å. Moreover, the observed reflection conditions are consistent with an I centring ($h + k + l = 2n$) for the basic lattice. There are nine orthorhombic space groups compatible with I centring ($I222$, $I2_12_12_1$, $Imm2$, $Ima2$, $Iba2$, $Immm$, $Imma$, $Ibam$ and $Ibca$); however, the ($2mm$) bright field (BF) symmetry observed in the $[1\bar{1}0]_o$ microdiffraction pattern of Fig. 9 is only compatible with the point group mmm (Morniroli & Steeds, 1992). Taking into account this point group, the extinction conditions exhibited require the space group $Immm$ for the basic structure. The modulation vector $\mathbf{q}$ is given here by $\mathbf{q} = (1 - \gamma)a*$.[1]

[1] The notation according to the *International Tables of Crystallography* (Hahn, 1992) should be $q = \gamma a*$; however, to correlate easily the composition with the γ value, as shown below, this modified notation is used instead.

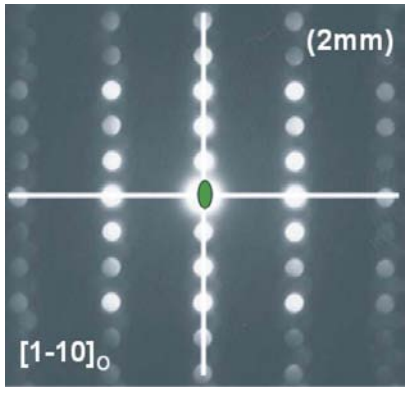

Figure 9
Microdiffraction pattern along the $[1\bar{1}0]_o$ zone axis. The bright field (BF) symmetry (2*mm*) is clearly observed.

The semiquantitative XEDS analysis of the composition over 30 different crystals showing modulation satellites yields an average composition $Bi_{4.2\ (3)}Fe_{0.5\ (2)}W_{0.4\ (2)}Br_{0.9\ (3)}$. The compositional ratio between Fe and W (∼1:1) has now changed with respect to the starting material, involving the presence of oxygen vacancies according to the next averaged nominal composition $Bi_4Fe_{1/2}W_{1/2}O_{8-\delta}Br$ ($\delta \simeq 0.25$), assuming that all the iron is present as Fe^{3+} and the tungsten as W^{6+}. We should bear in mind that this average composition comes from crystals with different γ values and therefore the ratio between Fe and W, as well as the Br and Bi contents, will vary in each crystal depending on how the structure accommodates those vacancies, as will be explained below.

The new unit cell of the modulated structure now presents the following parameters $a_{mod} = (1/\gamma)\ 3.8$, $b_{mod} = 3.8$ and $c_{mod} = 14.5$ Å.

Fig. 10 illustrates the respective indexing schemes in the four-dimensional superspace along $[010]_{mod} = [010]_o$ and $[001]_{mod} = [001]_o$ zone axes. For the $\gamma = 1/7$ diffraction pattern, the indexes of the commensurate $7a_{mod}, b_{mod}, c_{mod}$ supercell in the three-dimensional space group *Immm* are given in italics.

The systematic extinction condition associated with this one-dimensionally modulated structure is found to be

$$hklm : h + k + l = 2n + 1.$$

This extinction condition requires the average space group *Immm* and the superspace group $Immm[(1-\gamma)00]$ no. 71.1 for the modulated structure.

In Fig. 10 the SAED patterns are indexed on a four-dimensional basis. The irrational component $(1-\gamma)$ of the modulation vector **q** has been measured in different SAED patterns and we have found that it varies from one crystallite to another (Diaz & Hyde, 1983), ranging between 8/9 and 6/7 as shown in Fig. 11. This phenomenon has also been observed in the study of $Sr_4Fe_6O_{12+\delta}$, due to inhomogeneities in the oxygen distribution (Rossell *et al.*, 2004, 2005).

On the other hand, if we examine carefully the diffraction pattern along $[010]_{mod}$ (see Figs. 8 and 11), we note that at high *l* values of the *h*0*l* reflections the intensity of the satellite reflections increases in relation to the intensity of the basic structure reflections. This behaviour indicates that the modulation presents an important displacive transversal component along a_{mod} (Smith & Brown, 1988).

HRTEM image analysis: A HRTEM image of a modulated crystal with $\gamma = 0.11$ along $[010]_{mod}$ and the corresponding fast Fourier transform (FFT) are shown in Fig. 12(*a*). As the FFT shows, the structural modulation (satellite reflections) is present in the image together with the basic lattice (main reflections). Although the features of the modulation are clearly observed in the original HRTEM, in order to see more clearly the contrast that corresponds to the satellites and, therefore, the structural characteristics of the modulation, we have processed the image selecting the main reflections to reconstruct the basic lattice (Fig. 12*b*) and the satellites to reconstruct, by an inverse fast Fourier transform (IFFT), an image that contains only the structural modulation (Fig. 12*c*). Finally, these two processed images have been combined in a ratio of 1:3 to form a new processed image (Fig. 12*d*) where the intensity of the modulation has been increased three times with respect to the basic structure to enhance its characteristics.

The observed metric in the IFFT image from the basic structure is 3.8 Å × 14.5 Å (Fig. 12*b*). In the unprocessed image it is more difficult to differentiate between the contrast

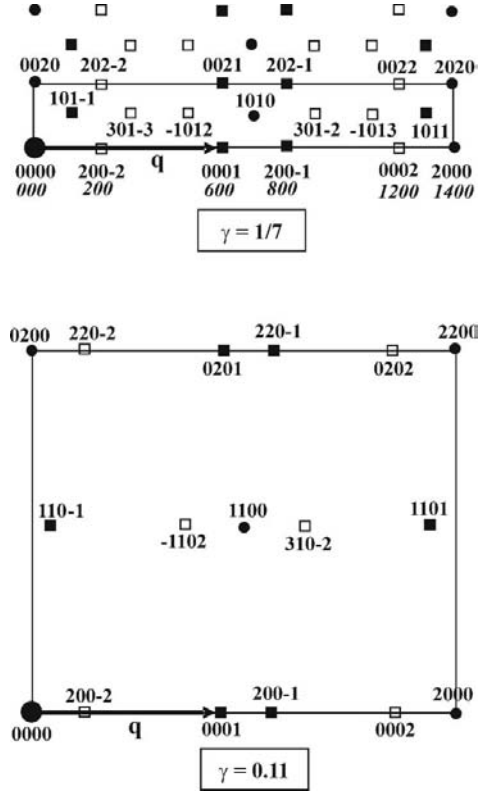

Figure 10
Indexing schemes of SAED patterns along the zone axes $[010]_{mod} = [010]_o$ (upper) and $[001]_{mod} = [001]_o$ (lower). The basic reflections are marked by black filled circles, whereas the first- and second-order satellites are marked by filled and empty black squares, respectively. The arrows indicate the modulation vector **q**. For the commensurate phase with $\gamma = 1/7$ the indexes of the supercell are written in italics.

from the bromine layer and that from the octahedral one. Once the image has been processed, with the intensity of the modulation increased threefold, the differences between these layers are observed (see Fig. 12*d*). The darker rows of dots correspond to the Bi_2O_2 sheets, which can also be inferred from the IFFT of the basic structure. We can also identify the dark dots surrounded by the disconnected bright ones with Br and those dark blobs surrounded in this case by less bright and connected dots with the $(Fe/W)O_6$ octahedra. They alternate in an almost regular sequence of five Br and four $(Fe/W)O_6$, yielding a ~ 34.2 Å $\times$ 14.5 Å supercell. This arrangement between the halogen and the octahedra allows the oxygen vacancies to be accommodated *via* the bonding $(Fe/W)O_5$—Br, since the Br from the neighbouring block compensates the oxygen vacancy in the $(Fe/W)O_{5+\square}$ square pyramid. A similar arrangement has been observed in the Bi–Sr–Fe–O system (Allix *et al.*, 2005). In the previous electron diffraction study, it was pointed out that, in addition to the compositional modulation, the structure also presents an important displacive component. This component is clearly observed in the processed HREM image of Fig. 12(*d*), where the dots marking the Bi_2O_2 layers exhibit a transversal wavy displacement running along *c*. These displacements are also clearly observed in the perspective of the original image (see Fig. 12*e*) where the wavy Bi_2O_2 layers are marked by yellow arrows, showing that although this feature is enhanced in the processed image it was already present in the original image and no artefacts are introduced by the image processing.

Fig. 13(*a*) displays an ideal model for this structure, approximating the modulation to a ninefold commensurate case, consisting of blocks projected along $[010]_{mod}$. The unit cell from the basic structure is outlined in red and the supercell caused by the alternation of five Br and four octahedra along *c* is outlined in black, leading to a new ninefold superstructure which is metrically close to the inverse of the γ value ($1/\gamma = 1/0.11 \sim 9$). We should not forget that a superstructure model is just a simplified commensurate approach to an incommensurate modulation, since, even if the latter can coincide metrically with a commensurate case, its incommensurability confers on the structure a qualitative difference (Withers *et al.*, 1998; Hansen *et al.*, 1995). Therefore, the proposed model is just a naive approximation to reality.

Since the oxygen vacancies can be accommodated by the bromine–octahedra bonding, we should point out that the thickness of one block Bi_2O_2–$(Fe/W)O_4$–Bi_2O_2 is 8.3 Å (Aurivillius), whereas it is 6.2 Å for the block Bi_2O_2–Br–Bi_2O_2 (Sillén). These differences result in a lateral mismatch between the alternating blocks. This misfit stress along both blocks is accommodated by the sinusoidal displacement of the Bi_2O_2 layers observed in the images and proposed in Fig. 13(*b*). Such a situation has also been found in bismuth high-temperature superconductors (Withers *et al.*, 1998; Hiraga *et al.*, 1988).

Using the projected model deduced from the HREM interpretation and taking into account the space group *Immm* and the unit-cell parameters of the ninefold superstructure, we can estimate the atomic coordinates. Placing the origin in the

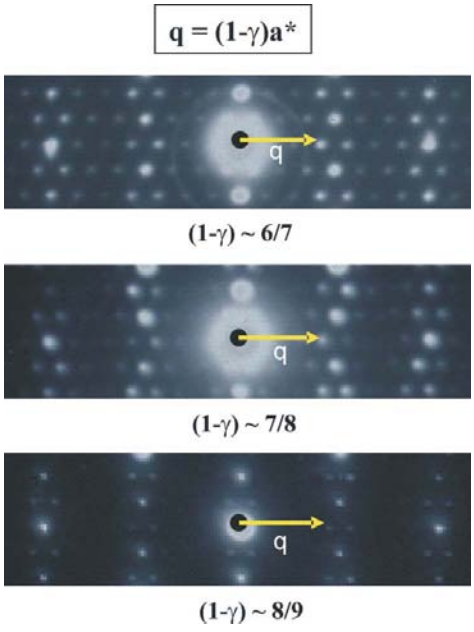

Figure 11
$[010]_{mod}$ electron diffraction patterns from different crystals showing $(1-\gamma)$ values of ~6/7, 7/8 and 8/9 marked by arrows.

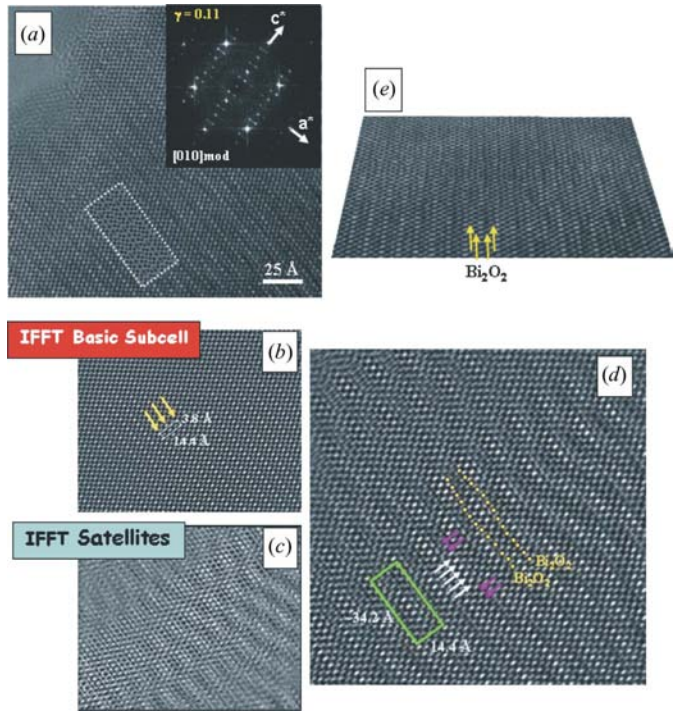

Figure 12
(*a*) HRTEM image along the zone axis $[010]_{mod}$ with $\gamma = 0.11$. (*b*) IFFT taking into account only the reflections from the basic subcell, indistinguishable bromine and octahedral layers are marked by yellow arrows. (*c*) IFFT masking only the satellite reflections. (*d*) Processed image composed by the IFFT of the basic cell and three times the IFFT using only the satellite reflections to enhance their effect. (*e*) HRTEM from (*a*) shown at glancing incidence. Note that the Bi_2O_2 rows marked by arrows follow a wavy trajectory.

Table 2
Measured coordinates from the HRTEM image along $[010]_{mod}$ with γ = 0.11.

*M*1* and *M*2* denote disordered Fe^{3+} and W^{6+} in these positions

Atom	Wyckoff	*x*	*y*	*z*
*M*1*	4(*e*)	0.0625	0	0
*M*2*	4(*e*)	0.1875	0	0
Br1	4(*e*)	3/8	0	0
Br2	4(*e*)	1/4	0	0
Br3	2(*b*)	1/2	0	0
Bi1	8(*m*)	0.22222	0	0.18
Bi2	8(*m*)	0.0555	1/2	0.37
Bi3	8(*m*)	0.1111	0	0.22
Bi4	8(*m*)	1/6	1/2	0.35
Bi5	4(*i*)	0	0	0.22
O1	2(*a*)	0	0	0
O2	4(*e*)	1/8	0	0
O3	4(*f*)	0.0625	1/2	0
O4	8(*m*)	0.1875	0	1/8
O5	8(*m*)	0.0625	0	1/8
O6	4(*f*)	0.1875	1/2	0
O7	4(*j*)	0	1/2	0.27
O8	8(*m*)	0.055	0	0.28
O9	8(*m*)	0.1111	1/2	0.27
O10	8(*m*)	1/6	0	1/4
O11	8(*m*)	0.222	1/2	1/4

equatorial oxygen of the octahedra and using symmetry relationships, the model obtained for this phase (see Fig. 13*c*) is displayed in Table 2. From this model is derived the composition $Bi_{18}M_4O_{33}Br_5$ (*M* = Fe, W), which is within the range of error measured in the average composition by XEDS.

High-resolution images were calculated based on the suggested model along $[010]_{mod}$. The calculated one with the defocus value of $\Delta f = -300$ Å and a crystal thickness of t = 15 Å was matched with the original image of Fig. 12(*a*) (see the insert in the lower-left corner of the micrograph). Notice that the structural model is proposed for a commensurate case. It may be observed that the calculated image consists of rows where five consecutive dark dots surrounded by four bright dots alternate with four dark dots surrounded in this case by four less bright and connected blobs. The experimental image is incommensurate, but it is possible to identify the same arrangement where dark dots surrounded by disconnected bright dots are followed by dark dots surrounded by connected bright dots, which corresponds to the arrangement of bromine and octahedra, respectively, as described above.

As was previously explained in the electron diffraction study, the value of γ can vary from one crystal to another ($\gamma \simeq$ 0.10–0.15), showing a behaviour typical of compositional modulated structures present in different systems, *i.e.* ytterbium sulfides (Diaz & Hyde, 1983). This variation is the result of the ordering between bromine and the octahedral layer with a different size. This hypothesis is confirmed in Fig. 14 which corresponds to a HRTEM image along $[010]_{mod}$ with γ = 0.10, that is a tenfold superstructure along *c* composed by the ordering of five bromines and five octahedra as can be observed in the image. The new supercell of $\sim$ 38 Å $\times$ 14.5 Å is outlined in the image and in the lower part of the figure a scheme of this structure made in blocks for this value of the modulation vector is displayed.

These experimental findings allow us to correlate the inverse of the γ value with the number of bromines (*m*) and octahedra (*n*) ordered to accommodate the oxygen vacancies ($1/\gamma = n + m$), but only after HRTEM studies will we be able to determine the values for *n* and *m*.

4. Conclusions

In this work we have investigated both the new structure of the $Bi_4Fe_{1/3}W_{2/3}O_8Br$ compound and the new phases obtained after a high-temperature treatment using the information that electron microscopy provides about reciprocal space, real space and the chemical composition of the crystals studied.

The $Bi_4Fe_{1/3}W_{2/3}O_8Br$ phase has been found to be isostructural with the $Bi_4Mn_{1/3}W_{2/3}O_8Cl$ and $Bi_4Ti_{1/2}W_{1/2}O_8Cl$ compounds; however, the expected doubling of the *c* axis previously found when bromine was inserted instead of chlorine in $Bi_4Ti_{1/2}W_{1/2}O_8Cl$ was not observed here. This is because the larger size of the transition metal ($^{VI}Fe^{3+}$ = 0.65 Å and $^{VI}Ti^{4+}$ = 0.61 Å; Shannon, 1976) makes the Aurivillius layer larger, on average. Therefore, the stress produced by the bromine into the Sillen's block is now smaller and does not give rise to the doubling of *c*. Besides, it seems that tetragonality tends to increase as one proceeds across the row of the 3*d*-transition metals, with the phase containing Ti^{4+} clearly orthorhombic from X-ray powder diffraction data and that containing Cu^{2+} tetragonal. The intermediate cations Mn^{3+} and Fe^{3+} exhibit a tetragonal unit cell taking into account only the X-ray data, but the electron diffraction experiments indicate that the true symmetry is orthorhombic in both cases. For this reason in these phases X-ray diffraction alone is not enough to determine the real symmetry, and therefore in this study electron diffraction and HRTEM are the main tools used to study the structure and defects.

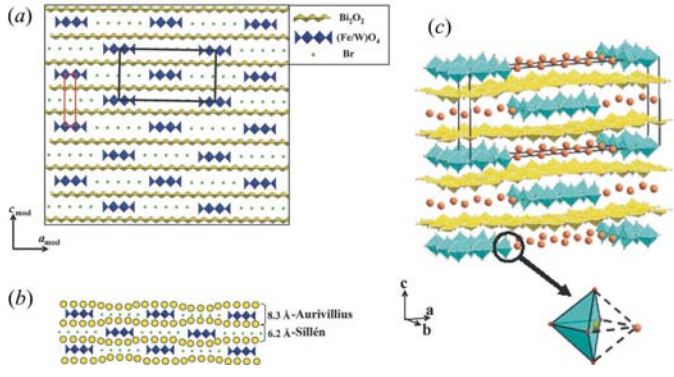

Figure 13
(*a*) Schematic structural model along $[010]_{mod}$ explaining how the compositional modulation is accommodated by the alternation of halide and perovskite blocks. (*b*) Schematic structural model explaining the origin of the displacive component of this modulation. (*c*) Three-dimensional model built up by the combination of HRTEM and crystallographic information.

The treatment of $Bi_4Fe_{1/3}W_{2/3}O_8Br$ at 1473 K yields crystals with extended defects that can be ordered, leading to the formation of new superstructures. These phases can be described as a new family of compounds with the general composition $(Bi_2O_2Br)[Bi_2Fe_{1/(2n+1)}W_{2n/(2n+1)}O_6]_n$, as was previously found in the study of $Bi_4Cu_{1/3}W_{2/3}O_{8-\delta}Cl$ as well as the opposite intergrowth $(Bi_2O_2Br)_n(Bi_2Fe_{2/3}W_{1/3}O_6)$.

Along with these superstructures, a new modulated structure originated by the accommodation of oxygen vacancies has been characterized, yielding structures in blocks where the value of γ defines the number of the alternating bromine and $(Fe/W)O_4$ blocks. As a consequence of this ordering, a displacive modulation is generated in the Bi_2O_2 layer to minimize the strains due to the lateral misfit between the two blocks.

This work was supported by the UCM–Santander project PR 27/05-13982. D. Ávila-Brande is grateful to Fundación Ramón Areces for a postdoctoral grant. The authors thank Professor Pérez Mato for help with the description of the superspace group.

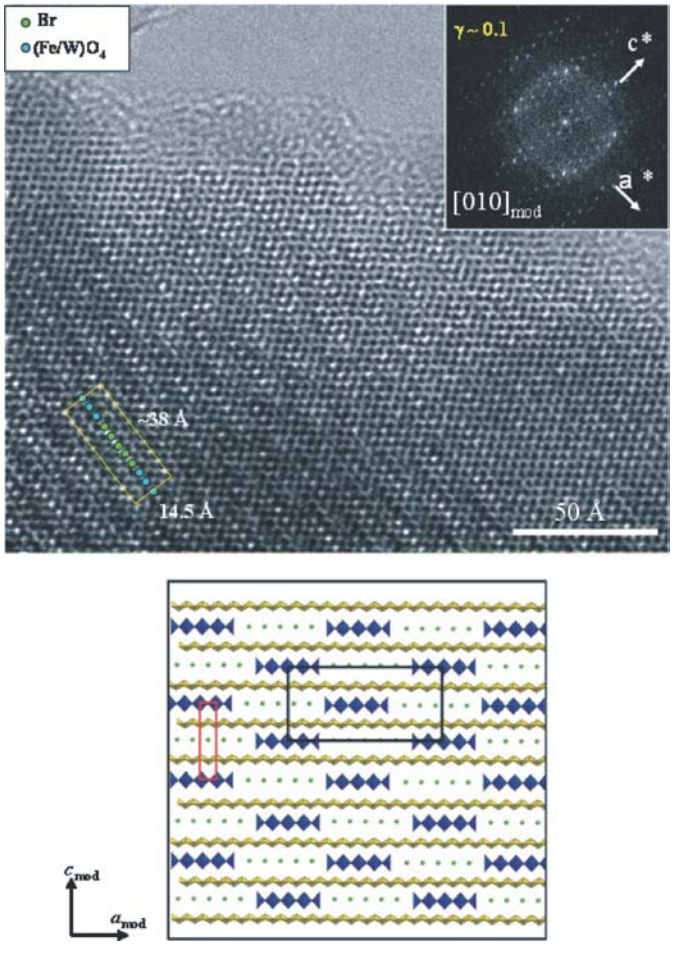

Figure 14
Experimental image from a different crystal along $[010]_{mod}$ with $\gamma = 0.10$, that is a tenfold superstructure formed by the ordering of five Br and five octahedral (marked with green and blue dots, respectively, in the image). The FFT is inset in the upper right corner. The structural model is depicted in the scheme displayed below.

References

Ackerman, J. F. (1986). *J. Solid State Chem.* **62**, 92–104.
Allix, M., Pelloquin, D. & Raveau, B. (2005). *J. Solid State Chem.* **178**, 1133–1138.
Aurivillius, B. (1949). *Ark. Kemi*, **1**, 463–480.
Aurivillius, B. (1984). *Chem. Scr.* **23**, 143–156.
Ávila-Brande, D. (2006). PhD thesis, Universidad Complutense, Spain.
Ávila-Brande, D., Gómez-Herrero, A., Landa-Cánovas, A. R. & Otero-Díaz, L. C. (2005). *Solid State Sci.* **7**, 486–496.
Ávila-Brande, D., Landa-Cánovas, A. R. & Otero-Díaz, L. C. (2007). *Chem. Mater.* **19**, 323–328.
Ávila-Brande, D., Landa-Cánovas, A. R., Otero-Díaz, L. C., Bals, S. & Van Tendeloo, G. (2006). *Eur. J. Inorg. Chem.* **9**, 1853–1858.
Bals, S., Van Aert, S., Van Tendeloo, G. & Ávila Brande, D. (2006). *Phys. Rev. Lett.* **96**, 096106.
Brauer, G. (1963). *Handbook of Preparative Inorganic Chemistry*, p. 624. London: Academic Press.
Diaz, C. O. & Hyde, B. G. (1983). *Acta Cryst.* B**39**, 569–575.
Gütlich, P. & Hauser, A. (1990). *Coord. Chem. Rev.* **97**, 1–22.
Hahn, T. (1992). *International Tables for Crystallography*, Vol. C, edited by A. J. C. Wilson. Dordrecht: Kluwer Academic Publishers.
Hansen, S., Landa-Cánovas, A., Ståhl, K. & Nilsson, J. (1995). *Acta Cryst.* A**51**, 514–519.
Hiraga, K., Hirabayashi, M., Kikuchi, M. & Syono, Y. (1988). *Jpn. J. Appl. Phys.* **27**, L573–L576.
Hyde, B. G., Thompson, J. G., Withers, R. L., Fitzgerald, J. G., Stewart, A. M., Bevan, D. J. M., Anderson, J. S., Bitmead, J. & Paterson, M. S. (1987). *Nature*, **327**, 402–403.
Kilaas, R. (1987). *Proceedings of the 45th Annual EMSA Meeting*, edited by G. W. Bailey, pp. 66–67. San Francisco, CA: San Francisco Press.
Kusainova, A. M., Stefanovich, S. Y., Dolgikh, V. A., Mosunov, A. V., Hervoches, C. H. & Lightfoot, P. (2001). *J. Mater. Chem.* **11**, 1141–1145.
Mitchell, R. H. (2002). *Perovskites Modern and Ancient*. Ontario, Canada: Almaz Press Inc.
Morniroli, J. P. & Steeds, J. W. (1992). *Ultramicroscopy*, **45**, 215–239.
Ourmazd, A., Rentschler, J. A., Spence, J. C. H., O'Keeffe, M., Graham, R. J., Johnson Jr, D. W. & Rhodes, W. W. (1987). *Nature*, **327**, 308–310.
Ramírez, A. P. (1997). *J. Phys. Condens. Matter*, **9**, 8171–8199.
Rossell, M. D., Abakumov, A. M., Van Tendeloo, G., Lomakov, V. L., Istomin, S. Y. & Antipov, E. V. (2005). *Chem. Mater.* **17**, 4717–4726.
Rossell, M. D., Abakumov, A. M., Van Tendeloo, G., Pardo, J. A. & Santiso, J. (2004). *Chem. Mater.* **16**, 2578–2584.
Scott, J. F. (1995). *Phys. World*, **8**, 46–50.
Scott, J. F. (1998). *Ferroelectr. Rev.* **1**, 1–130.
Shannon, R. D. (1976). *Acta Cryst.* A**32**, 751–767.
Smart, L. & Moore, E. (1992). *Solid State Chemistry: An Introduction*, p. 240. London: Chapman and Hall.
Smith, J. V. & Brown, W. L. (1988). *Crystal Structures, Physical, Chemical and Microtextural Properties*, Vol. 1, p. 76. Berlin: Springer-Verlag.
Tanaka, M. & Terauchi, M. (1985). *Convergent Beam Electron Diffraction*, pp. 153–155. Tokyo: JEOL Ltd.
Wells, A. F. (1975). *Structural Inorganic Chemistry*. Oxford: Clarendon Press.

Wilson, A. J. C. (1947). *Structure Reports*, Vol. 11. Oosthok: Utrecht, The Netherlands.
Withers, R. L. (1989). *Prog. Crystal Charact.* **18**, 139–204.
Withers, R. L., Schmid, S. & Thompson, J. G. (1998). *Prog. Solid State Chem.* **26**, 1–96.
Wolff, P. M. de, Janssen, T. & Janner, A. (1981). *Acta Cryst.* A**37**, 625–636.
Wu, M. K., Ashburn, J. R., Torng, C. J., Hor, P. H., Meng, R. L., Gao, L., Huang, Z. J., Wang, Y. Q. & Chu, C. W. (1987). *Phys. Rev. Lett.* **58**, 908–910.